

Simulation of photofission experiments at the ELI-NP facility



P. Constantin^{a,*}, D.L. Balabanski^a, P.V. Cuong^b

^aExtreme Light Infrastructure – Nuclear Physics, “Horia Hulubei” National Institute for Physics and Nuclear Engineering, Str. Reactorului 30, 077125 Bucharest Magurele, Romania

^bCentre of Nuclear Physics, Institute of Physics, Vietnam Academy of Science and Technology, Hanoi, Vietnam

ARTICLE INFO

Article history:

Received 15 September 2015

Received in revised form 5 January 2016

Accepted 1 February 2016

Keywords:

ELI-NP
Gamma beam
Photofission
Ion stopping
Ionic charge state

ABSTRACT

An extensive experimental program for the study of photofission will take place at the Extreme Light Infrastructure – Nuclear Physics (ELI-NP) facility, where different actinide targets will be exposed to a brilliant gamma beam to produce fission fragments. We report on the implementation within the Geant4 simulation toolkit of the photofission process, of related background processes, and of extended ionic charge parameterization. These developments are used to evaluate the production rates of photofission fragments and their release efficiency from the actinide targets.

© 2016 Elsevier B.V. All rights reserved.

1. Introduction

The ELI-NP facility will make available, in a few years, a gamma beam that will be a powerful and versatile tool for the study of various nuclear physics phenomena, like the photofission process [1]. Obtained by Compton backscattering (CBS) of a Yb:Yag laser beam with 0.4 J pulse energy on an intense electron beam accelerated up to about 720 MeV by a linear accelerator [2], this gamma beam will have a spectral density of up to $4 \cdot 10^4 / (s \cdot eV)$, an energy range of 0.2–19.5 MeV, a bandwidth (BW) of 0.3–0.5%, and a linear polarization above 99%.

These properties of the gamma beam offer the possibility to address several of the major open issues in our current understanding of fission. At energies below the fission barrier height (4–5 MeV), the bandwidth of 0.3% leads to energy resolutions of around 15 keV, allowing for the observation of individual transmission resonances in the fission isomeric shelf [3,4]. In this region, the investigation of the second and third minima of the fission potential barrier of super- and hyper-deformed actinides is of particular interest.

The measurement of angular distributions of photofission fragments, together with their mass, charge and kinetic energy, is another subject of interest within the ELI-NP research program, especially in rare fission modes like ternary fission. The small spot

size of the gamma beam provides good angular resolution and allows the construction of compact detectors.

The above measurements will be done by two state-of-the-art experimental setups which are designed at MTA Atomki (Hungary): a chain of five Bragg Ionization Chambers (BICs) [5], equipped with Double Sided Silicon Strip detectors (DSSSDs), and an array of thick Gas Electron Multiplier (THGEM) detectors [6].

Significant anisotropies have been observed in the orientation of the photofission fragments of ^{232}Th and ^{238}U in the 5–7.5 MeV beam energy range [7]. The high degree of polarization of the ELI-NP gamma beam will bring new insights into this effect. In addition, fission anisotropy provides an opportunity for measurements of nuclear g-factors of short-lived isomeric states in neutron-rich fission fragments, which cannot be accessed by other techniques. The nuclei of interest will be produced and implanted in a cubic host placed between the poles of a magnet.

These experiments will be performed with the ELIAD array which is under construction at ELI-NP and consists of large volume segmented HPGe Clover detectors coupled to fast-timing LaBr₃ crystals.

Finally, the energy range of the ELI-NP gamma beam covers the whole Giant Dipole Resonance (GDR) of Uranium and Thorium isotopes [8], and therefore is well suited for the production of exotic neutron-rich photofission fragments.

In order to extract and prepare radioactive ion beams (RIBs) with these fragments, and especially with the refractory elements in the Zr–Mo–Rh region of the light fragments with $A \approx 100$ and in the heavy rare-earth region around Ce of the heavy fragments with $A \approx 140$, an IGISOL facility will be constructed at ELI-NP. It will

* Corresponding author.

E-mail address: paul.constantin@eli-np.ro (P. Constantin).

contain a Cryogenic Stopping Cell (CSC) of the type which was recently developed at the GSI Institute (Germany) [9], where photofission fragments will be produced in Uranium targets, and the following devices: a Radiofrequency Quadrupole beam line that extracts, cools, separates on mass and bunches the ions from the CSC, an analyzing magnet and/or a Multiple-Reflection Time-of-Flight mass separator. The combined mass resolving power of the whole beam line will exceed 10^5 [10]. A measurement station comprising a β -decay tape-transport station and a γ spectrometer will be placed at its end.

All of the above experiments have at their core the use of a source of photofission fragments made by irradiating various actinide targets with the ELI-NP gamma beam. The work reported here uses simulations based on the Geant4 toolkit [22] to estimate the production and release rates of photofission fragments in the actinide targets used in all of the above mentioned experimental programs. The paper is organized as follows: Section 2 presents the ELI-NP gamma beam; Section 3 describes the implementation of the photofission process within Geant4 and the resulting photofission rates; Section 4 looks into the main background processes generated by the gamma beam in the targets; Section 5 describes the implementation of two new ionic charge state parameterizations into the existing Geant4 framework for ion stopping in matter; and Section 6 contains the results on the release efficiency and rates from the photofission ion sources.

2. The ELI-NP gamma beam

In the elastic approximation of the Compton process, the final energy E_γ of a photon with the initial energy E_L that scatters off a relativistic electron with the kinetic energy T_e is:

$$E_\gamma(\theta, T_e) = \frac{4\gamma_e^2 E_L}{(1 + \delta^2/4 + a_{op}^2/2) + \gamma_e^2 \theta^2} \quad (1)$$

where $\gamma_e = 1 + T_e/m_e c^2$ is the relativistic factor of the electron and θ is the photon scattering angle. A detailed presentation of CBS can be found in [2] and the references therein. The ELI-NP gamma beam uses a Yb:Yag green laser with the wavelength $\lambda = 515$ nm, corresponding to an incident photon energy $E_L = 2.4$ eV. The constant parameters in brackets are the laser incidence angle $\delta = 7.5^\circ = 0.131$ rad and the laser parameter $a_{op} = 4.3 (\lambda/w_0)\sqrt{U|J|/\sigma_t[ps]} = 0.041$, where we have used a typical set of laser parameters for the ELI-NP gamma beam: focal spot size $w_0 = 28$ μm , pulse energy $U = 0.4$ J and pulse time $\sigma_t = 1.5$ ps.

The upper limit of the gamma beam energy spectrum corresponds to forward scattered photons with $\theta = 0^\circ$ and, for the above set of parameters, is given by:

$$E_\gamma^{max}(T_e) = 9.55\text{eV} \cdot \left(1 + \frac{T_e}{m_e c^2}\right)^2 \quad (2)$$

The energy obtained with Eqs. (1) and (2) needs to be corrected down with a small recoil correction parameter $\Delta \approx 1\text{--}3\%$ [2], which represents the photon red shift due to the inelastic electron recoil.

In accordance with Eq. (2), the upper limit E_γ^{max} of the gamma spectrum can be adjusted by tuning the energy T_e of the electrons accelerated by the linac. For example, the gamma maximum energies $E_\gamma^{max} = 5.8$, 12.9 and 18.5 MeV are obtained for the electron energies $T_e = 400$, 600 and 720 MeV, respectively. The corresponding recoil corrections of $\Delta = 1.5\%$, 2.2% and 2.6% have been applied.

Due to its production via CBS, the ELI-NP gamma beam has a strong anti-correlation between its energy and emission angle, as can be seen in Eq. (1). This is used for the selection of the lower energy limit by beam collimation, as shown in Fig. 1. This figure displays the two types of beams that will be produced at ELI-NP:

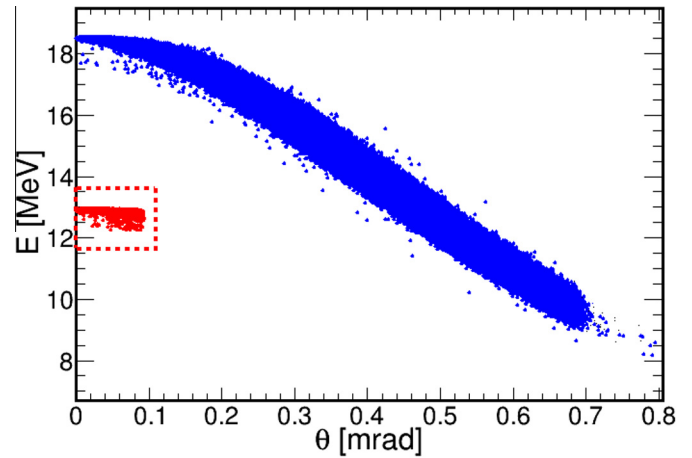


Fig. 1. Energy-angle correlation for two gamma beams: a broad beam up to 18.5 MeV collimated below 0.7 mrad (blue) and a pencil beam up to 12.9 MeV collimated below 0.09 mrad (red). The pencil beam is enclosed in a dashed red box for visibility. (For interpretation of the references to color in this figure legend, the reader is referred to the web version of this article.)

broad and pencil beams. The broad gamma beam with the energy range 10–18.5 MeV, shown with blue dots, was obtained by setting $T_e = 720$ MeV and collimating the beam below 0.7 mrad with a lead collimator. The pencil gamma beam with the narrow energy range around 12.9 MeV, shown with red dots and enclosed in a dashed red box, was obtained by setting $T_e = 600$ MeV and collimating the beam below 0.09 mrad. It has a root mean square (rms) of 65 keV, equal to the γ -ray nominal BW of 0.5% at 12.9 MeV.

Fig. 2 displays the two energy spectra obtained with the above procedure. The wide spectrum covers most of the GDR of actinides like ^{238}U and ^{232}Th , while the narrow spectrum demonstrates the standard 0.5% bandwidth of the ELI-NP gamma beam – the “pencil” beams with small energy and angular resolutions.

At 30 m from the CBS interaction point, where the BIC, THGEM and ELIADe setups will be located, pencil beams collimated to the nominal BW of 0.5% produce beam spots with the following one-dimensional rms: 2.0, 1.2 and 1.1 mm for $E_\gamma^{max} = 5.8$, 12.9 and 18.5 MeV, respectively. Further collimating the beam to the best BW of 0.3% reduces these beam spot rms to half of the above values. On the other hand, widening the collimator

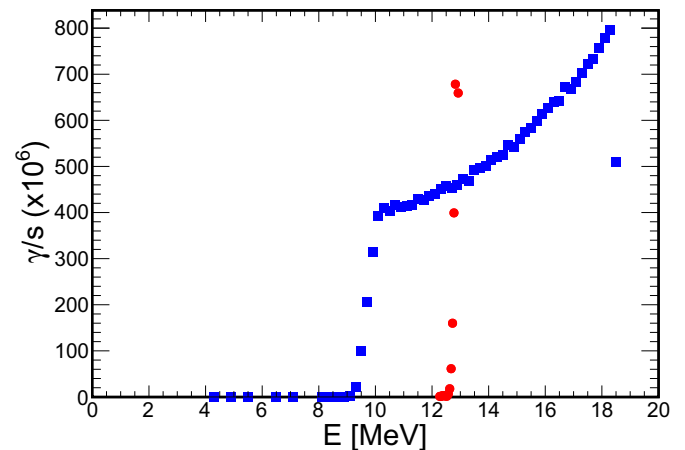


Fig. 2. The energy spectra of the broad beam between 10–18.5 MeV (blue squares) and of the pencil beam at $12.9 \pm 0.5\%$ MeV (red circles) from Fig. 1. (For interpretation of the references to color in this figure legend, the reader is referred to the web version of this article.)

aperture to get the 10–18.5 MeV broad beam shown in Figs. 1 and 2 results in a beam spot rms of 8 mm at the same location.

The capability of the ELI-NP gamma beam to be customizable to the particular needs of each experiment will be used by the photofission setups described here: studies of photofission transmission resonances with the BIC and THGEM arrays will use pencil beams, while production of exotic RIBs with the IGISOL beam line and of short-lived isomers for the ELIADÉ array will use broad energy beams.

Some photon background is produced in the collimator: electromagnetic processes in the material (lead or tungsten) and gammas scattered at or around the aperture hole. The level of this background varies somewhat with the collimator length and aperture, but was found to be less than 0.3% in all cases.

All the rates in our study have been normalized to a conservative value for the total gamma rate of $5 \cdot 10^{10} \gamma/s$ at the CBS interaction point, before collimation. This value is significantly lower than the expected rate of $10^{12} \gamma/s$ and we used it for rate estimates of day-one experiments.

3. Photofission simulation in Geant4

Gamma beams with the properties (energy spectrum, angular distribution, rate and flux) established as described above are used to irradiate, within the Geant4 Monte Carlo simulation framework [22], the target specific to each of the four experimental setups. The first aim is, of course, to estimate the fission rates. However, since the photofission process is not implemented in Geant4, the first step in our study is its implementation.

3.1. Photofission process implementation

The implementation in Geant4 of a physical process has two modules: the first calculates the interaction cross section and the mean free path in various materials, and the second generates the final state particles and their kinematic distributions. We have actually developed two independent implementations of the photofission process: both use the (γf) cross section parameterizations for various actinides from [8], but differ in their model for the distributions of final state products. In the low energy 5–7.5 MeV region, the $^{238}\text{U}(\gamma f)$ cross section from [3] was used.

In the first implementation, we use the final state model description of neutron induced fission below 60 MeV, based on evaluated (n, f) data libraries, available in Geant4 via the G4ParaFissionModel class. This code was validated to calculate the photofission yield in the case of the proposed ALTO gas cell [11], where the photon beam is produced via bremsstrahlung of a 50 MeV electron beam in a W converter and the target consists of four ^{238}U thin targets. We will refer henceforth to this implementation as the parafission model.

The second implementation defines the final state distributions from existing photofission measurements. The proton and neutron number (Z, N) distribution for the first fragment is taken from photofission measurements in ultra-peripheral $^{238}\text{U}(\gamma^* f)^{208}\text{Pb}$ collisions [12], where the energy of the virtual γ inducing the ^{238}U fission is below 25 MeV. Since these measurements were done up to $Z = 52$, an extrapolation based on Gaussian fits is used for higher Z elements. The prompt neutron multiplicity and energy distributions were implemented from bremsstrahlung photofission measurements reported in [13,14]. Then, the second fragment A and Z are computed using mass and charge conservation. Finally, fragment kinematics was generated using total kinetic energy data from [13,14] and energy and momentum conservation. The photofission fragment anisotropy reported in [7] was also included

in this final state model. We will refer henceforth to this implementation as the photofission model.

The parafission model brings reliability in our simulations because it uses a standard Geant4 class to generate the product kinematics of neutron induced fission, but with an appropriately modified cross section, and also because it has been tested against photofission data at ALTO. The photofission model brings precision in our simulations because it generates the product kinematics of photon induced fission from existing photofission measurements in the energy range relevant for the ELI-NP program.

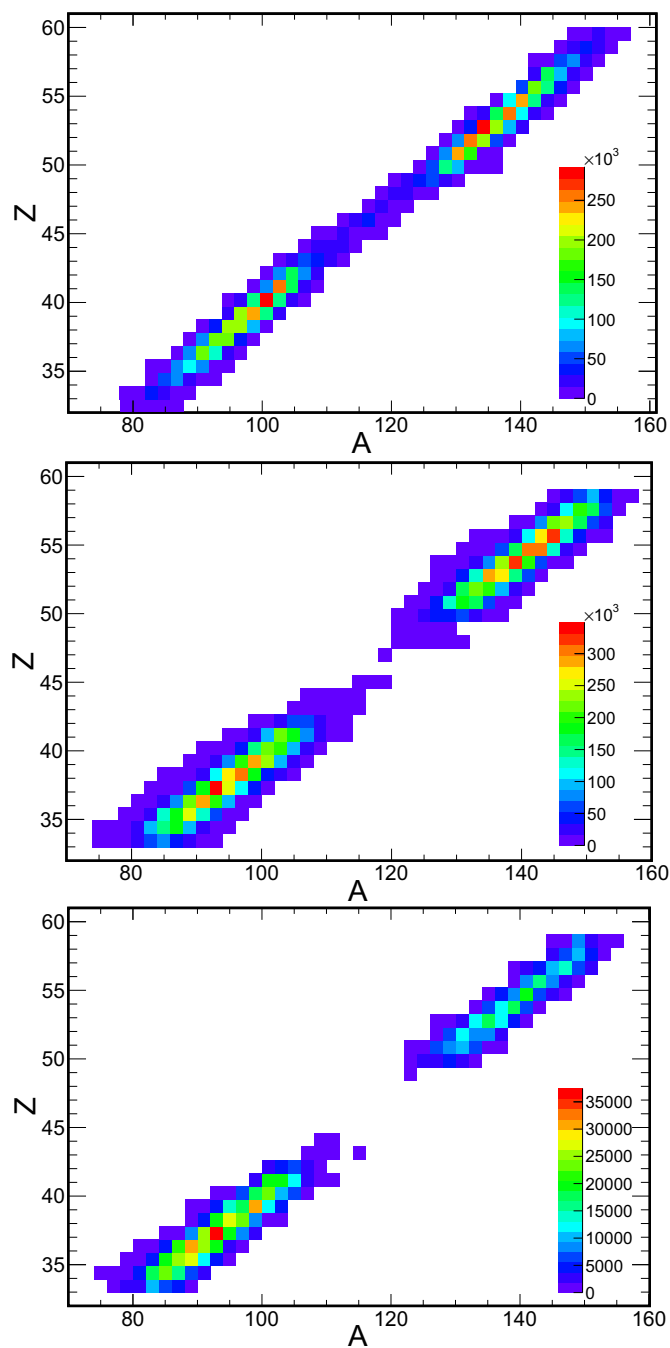


Fig. 3. Upper panel: nuclear charge Z versus atomic mass A of photofission fragments produced with the parafission model. Middle panel: nuclear charge Z versus atomic mass A of photofission fragments produced with the photofission model. Lower panel: nuclear charge Z versus atomic mass A of photofission fragments released from a 13 mg/cm^2 ^{238}U target with the photofission model and the Schiwietz q -parameterization (see Section 5.1).

Fig. 3 shows the atomic number Z versus the atomic mass A of the fission fragments generated with the two models described above: the upper panel uses the parafission model and the middle panel uses the photofission model. The upper and middle panels of Fig. 4 compare the kinetic energy KE versus the atomic mass A of the fragments generated with the two models. All panels in these two figures contain the fragments from the 10^7 fissions/s produced by exposing 800 mg of ^{238}U to a γ -ray with a total rate of $5 \cdot 10^{10} \gamma/\text{s}$ and the broad 10–18.5 MeV energy spectrum shown in Fig. 2. The lower Z limit in the middle panel of Fig. 3 corresponds to the lowest

element measured in [12], while the higher Z limit corresponds to the highest element where the extrapolation above $Z = 52$ is reliable. The lower panels will be explained and discussed later.

From Fig. 3, one difference that can be observed in the properties of the fission fragments generated with the two models is that the photofission model tends to produce slightly more fragments in the high Z and A region than the parafission model. The other difference noticeable in this figure is that the photofission model has a bigger isotopic spread than the parafission model. Regarding Fig. 4, there are only slight differences in the kinetic energy distributions of the two models.

In conclusion, since we do not study details of specific, limited regions of the nuclide chart in this report, these differences have very small impact on the type of results presented here. Moreover, it is the kinetic energy distribution that has the largest impact on phenomena studied here, like ion stopping, and these distributions differ very little.

3.2. Photofission rates

Table 1 lists the beam type and energy range and the target configuration used by each of the four experimental setups of the ELI-NP photofission program.

The BIC and THGEM setups use pencil beams (within the minimal 0.3% bandwidth), while the CSC and ELIADÉ setups use broad beams (within certain energy limits). Obviously, this implies that the gamma beam rate in the later two setups is significantly higher.

The BIC and THGEM targets use several thin foils amounting to a mass up to 7 mg, while the CSC and ELIADÉ targets use many thicker foils amounting to a mass up to 800 mg.

In nuclear moment measurements, the isomers of interest need to be implanted in a proper host lattice site. Having in mind the relatively low photofission cross-section ($\sim 10^{-24} \text{ cm}^2$), enough target material needs to be used. There are two options: a thick composite ^{238}U target with a proper lattice, for e.g. UIr_2 , or a stack of multilayer targets where the ^{238}U layer is sandwiched between layers of ferromagnetic material. In the second case, the thickness of the ^{238}U layers should be optimized such that the number of fission fragments that leave them and are implanted in the ferromagnetic host is maximized.

Hence, a large variety of beam energies, target masses, target foil thicknesses and configurations will be employed, leading to very different photofission rates:

- 10^7 fissions/s in the CSC target;
- $6 \cdot 10^4$ fissions/s in the ELIADÉ target;
- $(0.3\text{--}2) \cdot 10^3$ fissions/s in the THGEM target, depending on beam energy;
- 8 fissions/s in the BIC target.

Table 1

The four photofission experimental setups: beam energy, target total mass M , number of target foils N , foil thickness t , foil transversal size s and tilting angle α with respect to the beam axis. The BIC and THGEM setups use pencil beams (within the minimal 0.3% bandwidth), while CSC and ELIADÉ use broad beams (within certain energy limits).

	BIC	THGEM	CSC	ELIADÉ
E_γ [MeV]	5–6($\pm 0.3\%$)	5–19.5($\pm 0.3\%$)	10–19.5	5–7
Target	$^{238}\text{U}/^{232}\text{Th}$	$^{238}\text{U}/^{232}\text{Th}$	^{238}U	^{238}U
M [mg]	3.5–7	7	<800	800
N	5	10	15–30	100–500
t [mg/cm ²]	0.2–0.4	2	4–20	2–10
s [mm ²]	7.7×45	5×7	$6 \times (35\text{--}50)$	5×5
α	10°	5°	$7^\circ\text{--}10^\circ$	0°

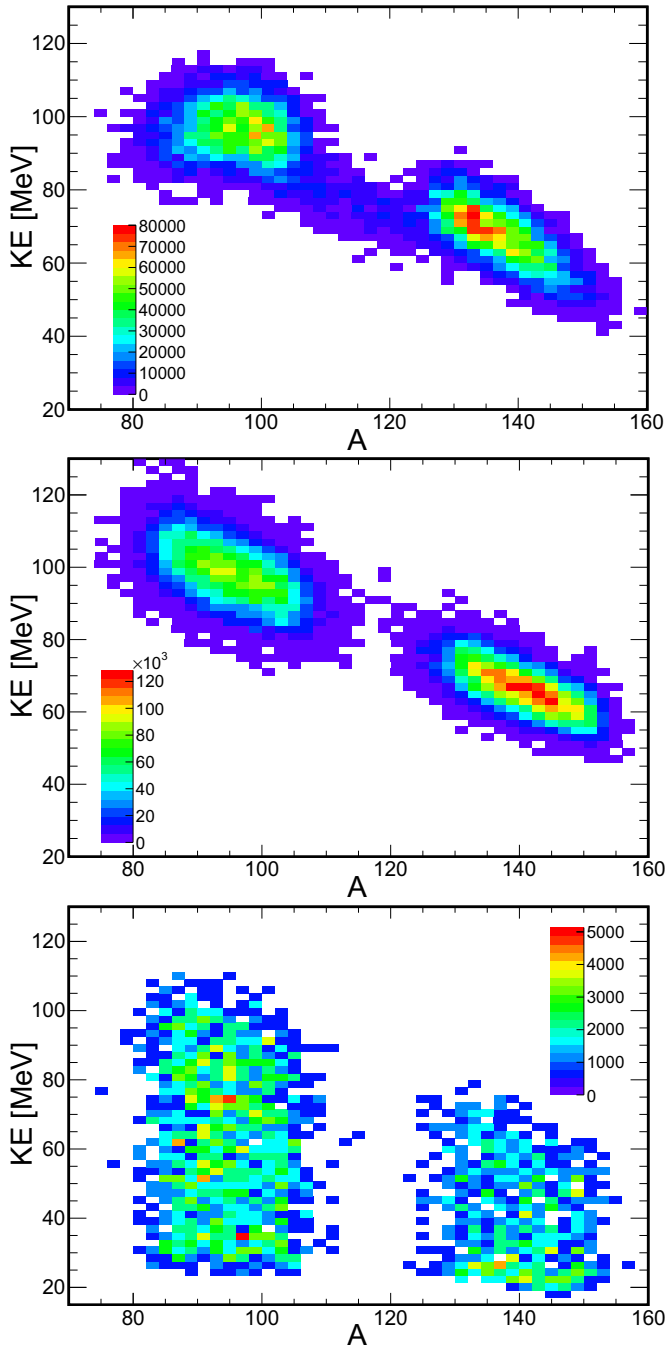


Fig. 4. Upper panel: kinetic energy KE versus atomic mass A of photofission fragments produced with the parafission model. Middle panel: kinetic energy KE versus atomic mass A of photofission fragments produced with the photofission model. Lower panel: kinetic energy KE versus atomic mass A of photofission fragments released from a 13 mg/cm^2 ^{238}U target with the photofission model and the Schwietz q -parameterization (see Section 5.1).

Consequently, the design of each detector setup should be adjusted to the expected fission yields which define the signal rates.

After accomplishing the first aim of the study, namely the estimation of the photofission rate for each experimental setup, we now move to the second aim: the estimation of the signal rates for each setup. The signal is formed by the fission fragments that manage to escape the stopping process inside the targets and are released. Before that, we will discuss the main background processes.

4. Background processes

Besides photofission, the gamma beam will generate other types of processes in the targets, namely electromagnetic (EM) processes and photo-nuclear processes. They become background sources in our devices. To study the effect of EM processes, the Geant4 standard and low energy EM physics classes were used. In the case of photo-nuclear processes, we have implemented our own (γ, n) and $(\gamma, 2n)$ processes within the Geant4 framework using the cross section measurements reported in [8]. Then, the subsequent neutron induced processes (elastic, inelastic, capture and fission) were addressed with the codes already available in Geant4.

In the case of the CSC setup, which has the largest target mass (together with the ELIADE setup) and the highest gamma beam rate, the simulated rate of neutrons produced by photonuclear (γ, n) and $(\gamma, 2n)$ reactions is $2 \cdot 10^7$ neutrons/s. This is not expected to be a significant background source.

The higher background contribution comes from gamma conversion into electrons in the target foils. In the case of the CSC setup, it amounts to about $7 \cdot 10^8$ e^+e^- pairs per second. But it is rather the secondary background effect of gas ionization by these electrons, which leads to avalanches of electron-ion pairs in the gas that surrounds the targets, that has the most important consequences. For this reason, this type of background will be addressed individually, for each of the four experimental setups, in separate dedicated reports.

5. Fragment stopping in the targets

The photofission fragments are generated, within the Geant4 framework, by the models described in Section 3.1 as fully ionized ions. Their subsequent transport in the target is then handled by the Geant4 classes for low energy electromagnetic interactions. More specifically, the electronic and nuclear ion stopping and multiple scattering effects are applied to their kinematic parameters.

The Bethe–Bloch energy loss formalism assumes that the ionic charge Q remains constant during stopping. This is true at large velocity v and low nuclear charge Z , because ions become quickly stripped of all their electrons. In general however, the ionic charge fluctuates during ion stopping in matter due to the competition between ionization and electron capture processes. The Bohr approximation $Q/Z \sim 1 - \exp(-v/v_B \cdot Z^{-2/3})$, where $v_B = 25$ keV/u is the electron Bohr velocity, can be used to describe these general features of the ionic charge evolution. We notice that fission fragments, with 0.3–1.5 MeV/u kinetic energy (see Fig. 4) and 30–60 nuclear charge (see Fig. 3), exhibit significant evolution of their ionic charge during stopping in matter. Hence, an accurate treatment of this phenomenon is essential.

Geant4 [22] implements the energy loss and ionic effective charge formalism from [15]: if S_p is the proton Bethe–Bloch stopping, the fractional ion effective charge γ is introduced in the ion stopping by $S = (\gamma Z)^2 S_p$. Brandt–Kitagawa theory gives $\gamma = q(1 + s.c.)$, where q is the fractional ion charge state $q = Q/Z$

and s.c. is a screening correction of the ion-medium interaction due to the electrons on ion's atomic shells.

5.1. Ionic charge state

The fractional ion charge state parameterization $q = q(v, Z, Z_{\text{targ}})$ has evolved in the last decades, taking more convoluted forms, as the volume of data measurements grew. To study its impact, we have added two parameterizations of q measurements to the one already implemented in the Geant4 class G4ionEffectiveCharge: the parameterization of Shima et al. [16], which is tailored for low energy ions, and the newer parameterization from Schiwietz and Grande [17] which includes a wider data set and differentiates between solid and gaseous targets. Note that only the ion charge state q changes between these parameterizations, the rest of the calculation of the ion effective charge γ and stopping power S according to [15] remaining the same.

Fig. 5 shows the distribution of the release rate of photofission fragments according to their ionic charge Q at the release moment from a 13 mg/cm^2 ^{238}U target. The three distributions correspond to the three q parameterizations mentioned above. Their mean and rms values are: $\langle Q \rangle = 9.8$ and $\sigma_Q = 3.0$ with the (default) Ziegler parameterization; $\langle Q \rangle = 16.5$ and $\sigma_Q = 2.0$ with the Shima parameterization; $\langle Q \rangle = 17.3$ and $\sigma_Q = 2.1$ with the Schiwietz parameterization.

Measurements with the LOHENGRIN spectrometer at ILL Grenoble of ionic charge state distributions in thermal neutron induced fission of ^{235}U [18] found $\langle Q \rangle = 20\text{--}22$ and $\sigma_Q = 2.0\text{--}2.4$. Similar values were measured in $^{239}\text{Pu}(n_{\text{th}}, f)$ [19], $^{241}\text{Am}(2n_{\text{th}}, f)$ [20] and $^{241}\text{Pu}(n_{\text{th}}, f)$ [21]. These values refer to the regular ionic charge state distributions, unaffected by the presence of nanosecond isomeric states. When such isomers are present, they decay by conversion with electrons from internal shells and the produced vacancies lead to Auger cascades and, consequently, to ionic charge states higher by $\Delta(Q) \approx 3$ [18].

Fig. 6 shows the dependence of the ionic charge Q , at the moment of release from the target, on the ion velocity v for five values of the nuclear charge $Z = 36, 38, 40, 56, 58$. The lower set of five tightly bound curves, drawn with open circles, is produced with the Ziegler parameterization, while the upper set of five loosely bound curves, drawn with full squares, is produced with the Schiwietz parameterization. Apart from the overall higher Q values, the Schiwietz parameterization has also a more pronounced dependence on the nuclear charge Z than the Ziegler

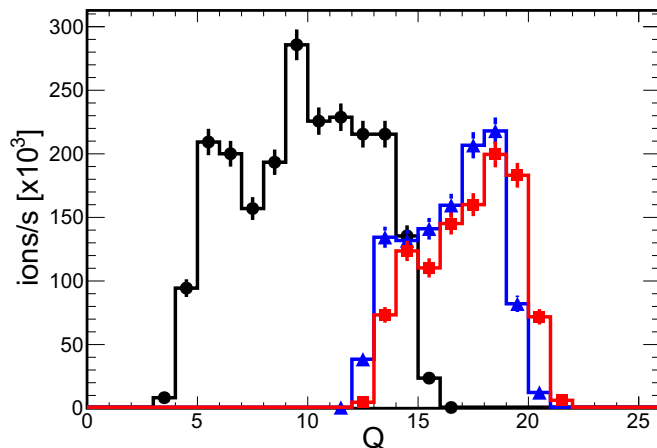


Fig. 5. The dependence of fragment release rate from a 13 mg/cm^2 ^{238}U target on the ionic charge Q with Ziegler (black circles), Shima (blue triangles) and Schiwietz (red squares) parameterizations of the ionic charge state q . (For interpretation of the references to color in this figure legend, the reader is referred to the web version of this article.)

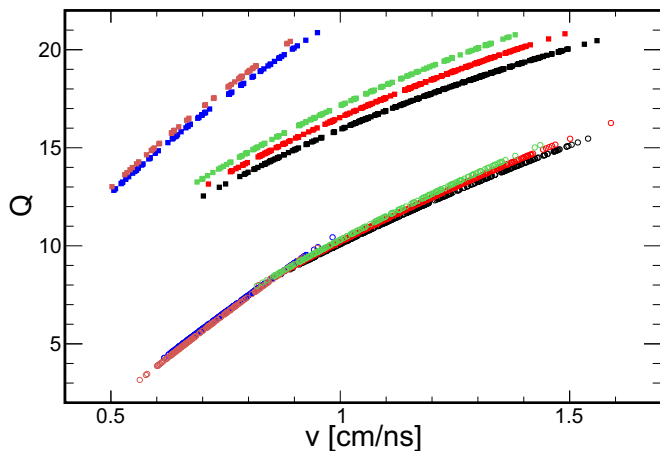


Fig. 6. Ionic charge versus velocity for fission fragments released from a 13 mg/cm² ²³⁸U target with Ziegler (open circles) and Schiwietz (full squares) parameterizations for five nuclear charges: $Z = 36$ (black), $Z = 38$ (red), $Z = 40$ (green), $Z = 56$ (blue), $Z = 58$ (brown). (For interpretation of the references to color in this figure legend, the reader is referred to the web version of this article.)

parameterization. The curves with the Shima parameterization, not shown in this figure for clarity, follow closely those with the Schiwietz parameterization.

Measured values of ionic charge dependence on ion velocity v (Fig. 5 in [18]) show an increase in both mean value and slope between the Kr ($Z = 36$) and Sr ($Z = 38$) isotopes in the region $v \approx 1.40$ – 1.48 cm/ns, if one excludes the nuclides which are assumed to be influenced by internal conversion. Comparing with the corresponding black and red curves in Fig. 6, one sees that this is closer to the $Q(v)$ variation with Z in the Schiwietz parameterization (full squares) than to that in the Ziegler parameterization (open circles).

In conclusion, Shima and Schiwietz q parameterizations produce ionic charge states that are close to each other and are much closer to the measured values than the default Ziegler parameterization of Geant4. There is still a discrepancy of about 15% between $\langle Q \rangle$ with the new parameterizations and the measured values. The spread σ_Q with the new parameterizations agrees with the measured one, while that with the Ziegler parameterization is larger. We note that, as discussed in [18], a precise description of the ionic charge evolution involves taking into account the effect of internal conversions followed by Auger cascades and is beyond the scope of the work presented here. Hence, for the rest of the simulations, we use the Schiwietz parameterization as our baseline and include the above discrepancy as a systematic error.

5.2. Properties of the released fragments

After their production in the actinide targets, fragments lose energy in the target material and some escape and get released in the surrounding gas. This can be seen in the lower panel of Fig. 4, which should be compared with its middle panel, where the kinetic energy KE of the fragments released from a 13 mg/cm² foil of an ²³⁸U target is plotted against their atomic mass A . The Schiwietz q -parameterization was used in this panel. Apart from the overall decrease in the total number of fragments, the shape of the kinetic energy distribution changes: the mean value decreases from 82.5 MeV to 56.3 MeV and the rms value increases from 17.6 MeV to 22.1 MeV. Also, the characteristic double-humped structure disappears from the KE distribution of the released fragments.

Regarding the nuclear charge Z and the atomic mass A distributions of the released fragments, one can see by comparing the

lower and middle panels of Fig. 3 that the stopping with the Schiwietz q -parameterization is stronger for the heavy fragment region than for the light fragment region: if the heavy to light yield ratio is one at their production moment (upper and middle panels), it becomes about 0.45 at their release moment (lower panel). On the other hand, performing the stopping with the Ziegler q -parameterization preserves the equal distribution of the fragments between the heavy and light regions. This behavior is a consequence of the fact that ion stopping is, to first order, proportional to Q^2/v^2 and, considering the ionic charge dependence on velocity shown in Fig. 6, it becomes evident that the Schiwietz q -parameterization will produce an ion stopping much more dependent on the nuclear charge Z than the Ziegler q -parameterization.

Fig. 7 shows the distribution of two types of ion rates according to their path length δ in the ²³⁸U target: the production rate of photofission fragments with green squares and the release rate of photofission fragments with black circles. The Ziegler q -parameterization was used in this figure. All fragments that travel less than about $\delta \approx 3.2$ mg/cm² escape outside the target. The release rate decreases by an order of magnitude, compared to the plateau value, when the path length becomes $\delta \approx 5$ mg/cm².

Fig. 8 shows exactly the same distributions as Fig. 7, except that the Schiwietz q -parameterization is used instead. This time, all fragments that travel less than about $\delta \approx 1$ mg/cm² escape outside the target. The release rate decreases by an order of magnitude when the path length becomes $\delta \approx 3.2$ mg/cm². As before, the distribution using the Shima q -parameterization lies close to the one using Schiwietz.

Fig. 9 shows the path length δ distribution, with the Schiwietz q -parameterization, of the released fragments from the heavy and light regions in blue and red, respectively. Their sum is, of course, the distribution in black in Fig. 8. The significant dependence of the ion stopping with this parameterization on the nuclear charge Z is the cause for this behavior. No difference is seen between the corresponding δ distributions made for light and heavy ions with the Ziegler q -parameterization.

The more than 30% decrease in the path length of the photofission fragments inside the target, when switching from the Ziegler q -parameterization to the Schiwietz q -parameterization, comes from the faster ionic charge decrease in the first case: fragments start fully stripped ($Q = Z = 30$ – 60) at their production moment and decrease their charge to $Q = 5$ – 15 with the Ziegler

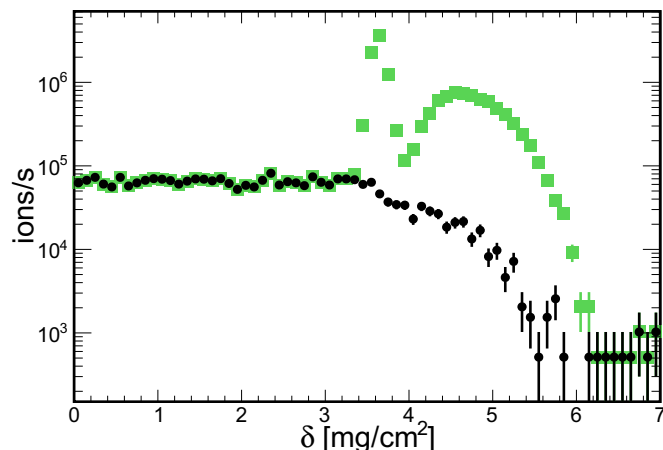


Fig. 7. Path length in the target of all fragments (green squares) and of the released fragments (black circles) with the Ziegler parameterization. (For interpretation of the references to color in this figure legend, the reader is referred to the web version of this article.)

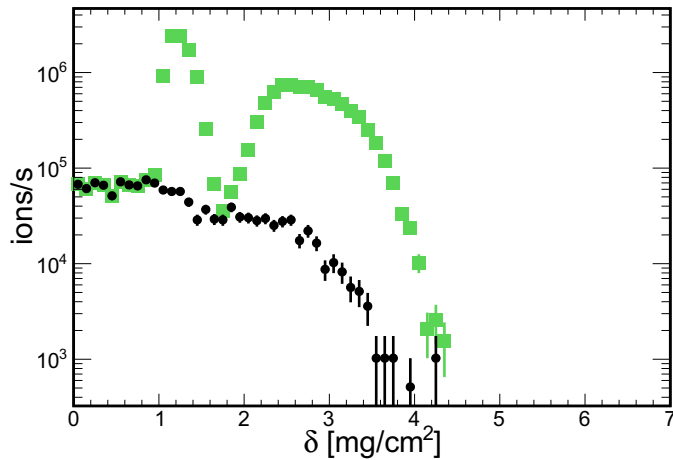


Fig. 8. Same as Fig. 7, but with the Schiwietz parameterization.

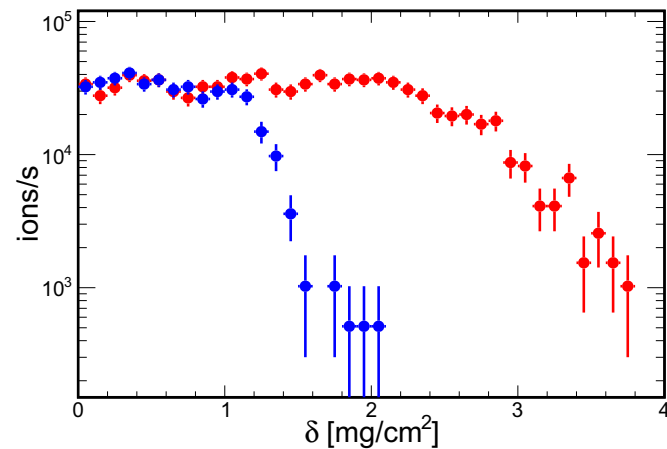


Fig. 9. Path length in the target of the released fragments from the heavy region (blue) and from the light region (red), with the Schiwietz parameterization. (For interpretation of the references to color in this figure legend, the reader is referred to the web version of this article.)

parameterization and to $Q = 12$ – 22 with the Schiwietz parameterization until they exit the target (see Fig. 5).

The double-humped structure of the fragment production rates present in the above δ distributions comes from the double-humped structure of the initial kinetic energy of the fission fragments (see Fig. 4). To establish this, we looked at the (KE, A) distributions of the fragments that are stopped using the Schiwietz parameterization in the three regions for the path length δ shown in Fig. 8 with green squares: 0 – 1 , 1 – 1.7 and above 1.7 mg/cm^2 . The fragments from the first δ interval come equally from the light and heavy regions, those from the second δ interval come almost exclusively from the heavy region and those from the third interval come from the light region.

We have also looked at the angular distribution of the released fragments with respect to the target and found that it is fairly uniform, with the exception of a depletion at the very shallow emission angles (parallel emission).

6. Fragment release efficiency and rates

We can now estimate the rates at which the targets, acting as sources of photofission fragments placed in the center of the experimental setups, release the signal ions.

In a first step, we quantify the stopping of the photofission fragments in the target material by introducing the single release efficiency as the percentage of the produced ions that are released and the pair release efficiency as the percentage of the produced ion pairs (from the same fission process) that are released as a pair.

Fig. 10 shows the dependence of the single ion release efficiency on the nuclear charge Z with the Schiwietz q -parameterization with black circles and with the Ziegler q -parameterization with blue triangles, for a ^{238}U target with 13 mg/cm^2 thickness. In line with the discussions above, we get a monotonic decrease of the efficiency with the nuclear charge (and mass) of the ions in the first case and an independence in the second case.

Fig. 11 shows the single release efficiency with black circles and the pair release efficiency with red squares, with the Schiwietz parameterization, as a function of the target foil thickness. These values can also be viewed in Table 2. While the single efficiency drops fast to about 20% at $t \approx 6$ mg/cm^2 and then has a slow decrease reaching about 5% at $t \approx 20$ mg/cm^2 , the pair efficiency has an even faster decrease and becomes null around $t \approx 4$ mg/cm^2 .

This behavior is a consequence of the path length distributions of the released ions shown in Figs. 8 and 9. For the single ion release efficiency, it is the two sides of the target surface that contribute, and each does it separately up to a depth of about 3 mg/cm^2 . For the pair release efficiency both back-to-back ions must be released, hence the maximum thickness is about twice the size of the plateau region in Fig. 9.

The single release efficiency shown with blue triangles in Fig. 11 is obtained using the Ziegler q -parameterization and is about twice higher than that with the Schiwietz q -parameterization for foil thicknesses larger than 4 mg/cm^2 (see last column in Table 2).

There is an approximate linear and quadratic decrease of the single and pair efficiencies, respectively, with the mean ionic charge $\langle Q \rangle$. Using this dependence, we estimate the systematic errors of the release efficiencies in Table 2, starting from the $\langle Q \rangle$ discrepancy of 15% between the measured values and those with the Schiwietz q -parameterization discussed at the end of Section 5.1.

Devices like the BIC or THGEM arrays, which study pairs of photofission fragments, must employ a foil thickness below 3 mg/cm^2 in order to have a significant counting rate. On the other hand, devices that study uncorrelated fragments, like CSC and ELIADÉ, can use larger foil thicknesses and need to optimize the overall target geometry for maximum counting rates.

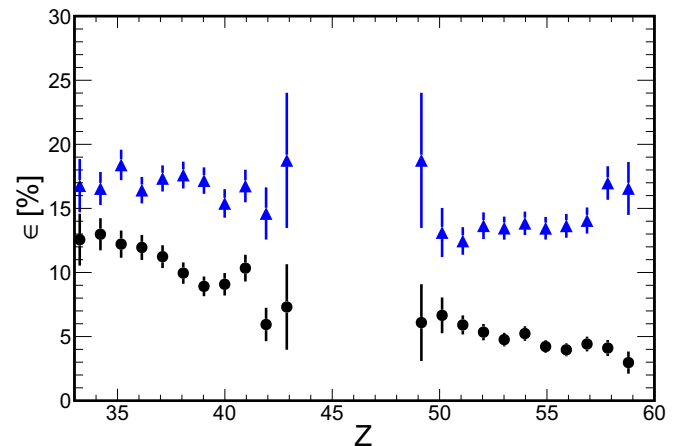


Fig. 10. Single release efficiency versus nuclear charge Z with the Schiwietz parameterization (black circles) and with the Ziegler parameterization (blue triangles). (For interpretation of the references to color in this figure legend, the reader is referred to the web version of this article.)

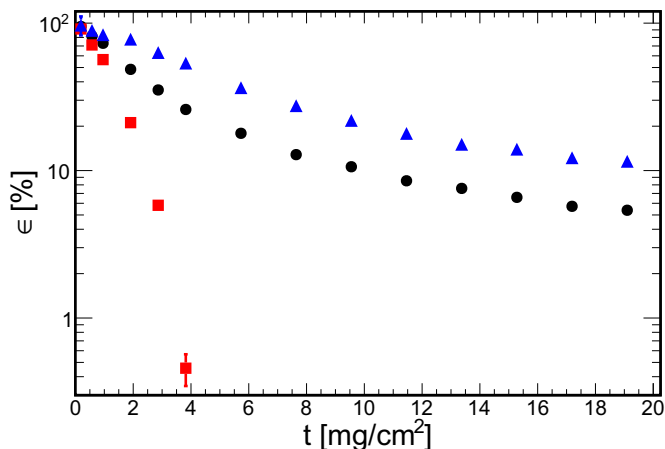


Fig. 11. Single release efficiency with Schiwietz parameterization (black circles) and with Ziegler parameterization (blue triangles), and pair release efficiency with Schiwietz parameterization (red squares). (For interpretation of the references to color in this figure legend, the reader is referred to the web version of this article.)

Table 2

Release efficiency (with Schiwietz parameterization): target foil thickness in the first column (in μm for ^{238}U), single release efficiency in the second column and pair release efficiency in the third column. The first (symmetric) error is statistical and the second (negative) error is systematic, due to ionic charge state variation. The fourth column shows the ratio between the single efficiency with the Schiwietz q -parameterization and that with the Ziegler q -parameterization.

Thickness	Single efficiency [%]	Pair efficiency [%]	Ratio
0.19 mg/cm ² (0.1 μm)	94.9 \pm 4.7–0.7	91.3 \pm 5.7–0.6	0.98 \pm 0.07
0.57 mg/cm ² (0.3 μm)	81.5 \pm 4.3–2.8	71.1 \pm 5.1–1.7	0.91 \pm 0.07
0.96 mg/cm ² (0.5 μm)	73.0 \pm 1.8–3.8	56.6 \pm 1.9–2.4	0.87 \pm 0.03
1.91 mg/cm ² (1 μm)	48.6 \pm 1.0–10.5	21.1 \pm 0.8–5.8	0.62 \pm 0.02
2.87 mg/cm ² (1.5 μm)	35.2 \pm 0.8–10.1	5.8 \pm 0.4–5.3	0.55 \pm 0.02
3.82 mg/cm ² (2 μm)	26.0 \pm 0.7–9.9	0.5 \pm 0.1–0.5	0.48 \pm 0.01
5.73 mg/cm ² (3 μm)	17.9 \pm 0.5–6.7	0	0.49 \pm 0.01
7.64 mg/cm ² (4 μm)	12.8 \pm 0.4–5.3	0	0.47 \pm 0.02
9.55 mg/cm ² (5 μm)	10.6 \pm 0.4–4.0	0	0.49 \pm 0.02
11.5 mg/cm ² (6 μm)	8.5 \pm 0.3–3.3	0	0.48 \pm 0.02
13.4 mg/cm ² (7 μm)	7.6 \pm 0.3–2.7	0	0.50 \pm 0.02
15.3 mg/cm ² (8 μm)	6.6 \pm 0.3–2.6	0	0.47 \pm 0.02
17.2 mg/cm ² (9 μm)	5.7 \pm 0.3–2.3	0	0.47 \pm 0.02
19.1 mg/cm ² (10 μm)	5.4 \pm 0.3–2.2	0	0.47 \pm 0.02

Using the thickness values listed in Table 1, the release efficiencies listed in Table 2 and the photofission rates listed at the end of Section 3.2, we obtain the following release rates:

- (0.6–2.2)·10⁶ fragments/s in the CSC;
- (0.7–6)·10⁴ fragments/s in the ELIADÉ array;
- (0.1–1.2)·10³ pairs/s in the THGEM array;
- 6–8 pairs/s in the BIC array.

for a gamma beam rate of $5 \cdot 10^{10}$ γ /s.

All the systematic and statistical errors from Table 2 were propagated in the ranges of the above rates.

7. Conclusions and outlook

In order to evaluate the performance of the various targets of our experimental setups as photofission ion sources, we have implemented the photofission process of several actinides and two new parameterizations of the ionic charge state in the Geant4 simulation framework. This has allowed us to: calculate the photofission rates in these targets; study in detail the properties of the released fragments; estimate the dependence of single and pair release efficiencies on the target foil thickness and, finally, the fragment release rate in each setup.

Of course, this study needs to be continued individually for each of the four setups. In particular, the next steps are: finding to optimized target geometry that maximizes the above rates; stopping and ionization effects of the released fragments in the gas volume of each setup; study of the signal and background generation in each case.

Acknowledgements

The Extreme Light Infrastructure Nuclear Physics (ELI-NP) – Phase I project is co-funded by the European Union through the European Regional Development Fund. Phan Viet Cuong acknowledges the support of the Vietnam National Foundation for Science and Technology Development (NAFOSTED) under Grant No. 103.04-2014.29.

References

- [1] D.L. Balabanski et al., *J. Phys. Conf. Series* 590 (2015) 012005; D.L. Balabanski, *Pramana* 83 (2014) 713.
- [2] O. Adriani et al., arXiv:1407.3669 (2014).
- [3] L. Csige et al., *Phys. Rev. C* 87 (2013) 044321.
- [4] P.G. Thirolf et al., *EPJ Web Conf.* 38 (2012) 08001.
- [5] C. Budtz-Jorgensen et al., *Nucl. Instr. Meth. A* 258 (1987) 209.
- [6] C.K. Shalem et al., *Nucl. Instr. Meth. A* 558 (2006) 468.
- [7] J.M. Mueller et al., *Phys. Rev. C* 89 (2012) 034615.
- [8] J.T. Caldwell et al., *Phys. Rev. C* 21 (1980) 1215.
- [9] M. Ranjan et al., *Nucl. Instr. Meth. A* 770 (2015) 87.
- [10] W.R. Plass et al., *Nucl. Instr. Meth. B* 317 (2013) 457.
- [11] P.V. Cuong, Development of a new surface ion-source and ion guide in the ALTO project, Diploma thesis, University Paris XI Orsay (2009).
- [12] C. Donzaud et al., *Eur. Phys. J. A* 1 (1998) 407.
- [13] S. Pomme et al., *Nucl. Phys. A* 572 (1994) 237.
- [14] M. Piessens et al., *Nucl. Phys. A* 556 (1993) 88.
- [15] J.F. Ziegler, J.M. Manoyan, *Nucl. Instr. Meth. B* 35 (1988) 215; J.F. Ziegler, J.P. Biersack, U. Littmark, *The Stopping and Range of Ions in Matter*, Vol. 1, Pergamon Press, 1985.
- [16] K. Shima et al., *Nucl. Instr. Meth.* 200 (1982) 605.
- [17] G. Schiwietz, P.L. Grande, *Nucl. Instr. Meth. B* 175–177 (2001) 125.
- [18] H. Wohlfarth et al., *Zeitschr. Phys. A* 287 (1978) 153.
- [19] C. Schmitt et al., *Nucl. Phys. A* 430 (1984) 21.
- [20] C. Amouroux et al., *EPJ Web Conf.* 62 (2013) 06002.
- [21] A.D. Belyaev et al., *Nucl. Instr. Meth. B* 43 (1989) 5.
- [22] S. Agostinelli et al., *Nucl. Instr. Meth. A* 506 (2003) 250.